Predicting the Compression-After-Impact (CAI) strength of damage-tolerant hybrid unidirectional/woven carbon-fibre reinforced composite laminates

Published in:
Composites Part A: Applied Science and Manufacturing

Document Version:
Peer reviewed version

Queen's University Belfast - Research Portal:
Link to publication record in Queen's University Belfast Research Portal

Predicting the Compression-After-Impact (CAI) strength of damage-tolerant hybrid unidirectional/woven carbon-fibre reinforced composite laminates

Haibao Liu[a], Brian G. Falzon[a]*, Wei Tan[b]

[a] *School of Mechanical and Aerospace Engineering, Queen`s University Belfast, Ashby Building, Belfast BT9 5AH, UK*

[b] *Engineering Department, University of Cambridge, Trumpington Street, Cambridge CB2 1PZ, UK*

ABSTRACT

The evaluation of Compression-After-Impact (CAI) strength is of great significance in the design of composite aerostructures. This paper presents a model for the numerical simulation of Compression-After-Impact (CAI) of hybrid unidirectional (UD)/woven carbon-fibre reinforced composite laminates. This three-dimensional damage model is based on Continuum Damage Mechanics (CDM) and Linear Elastic Fracture Mechanics (LEFM), and implemented as a user defined material subroutine (VUMAT) in Abaqus/Explicit. This model, which accounts for interlaminar and intralaminar damage, and load reversal, incorporates a non-linear shear profile to account for matrix plasticity. Two different composite laminate lay-ups with varying extent of initial impact damage were tested to validate the computational model and enable a quantitative study of the influence of using woven plies on the surfaces of a laminate. Woven surface plies are often used in composite aerostructures to mitigate damage during drilling and constrain the extent of damage during low velocity impact. Good correlation was obtained between physical testing and simulation results, which establishes the capability of this damage model in predicting the structural response of composite laminates. The fully validated model was used to compare the Compression-After-Impact (CAI) strength of an equivalent unidirectional (UD)-only carbon-fibre reinforced composite laminate. The results showed that the hybrid unidirectional (UD)/woven laminate had a marginally higher strength (+3.3%) than the equivalent unidirectional (UD)-only laminate.

Keywords: A. Laminates; B. Strength; C. Finite Element Analysis (FEA); D. Mechanical testing;

1. Introduction

Carbon-fibre reinforced composite laminates are increasingly used in aerostructures, primarily because of their excellent high specific strength and stiffness, and good fatigue resistance. However, carbon-fibre/epoxy composites do have their own drawbacks. For example, the weak through-thickness strength in laminated structures makes them susceptible to impact damage [1,2]. Moreover, induced damage may not be visible but may, nonetheless, significantly reduce a laminate`s residual compressive strength. Consequently, a better understanding of the behaviour of post-impacted laminates under compressive loading is essential for the design and maintenance of composite structures [3–6].

In the design of composite aerostructures, the residual strength is usually investigated by performing compressive tests on damaged specimens impacted at different energy levels [7,8]. While a number of 'in-house' and standardised tests have been adopted (e.g. [9,10]), they each share the same basic approach. Pristine samples are tested in a drop-weight impact testing machine to generate a certain degree of damage within the laminates. The resulting damaged samples are then clamped within a support fixture, and loaded in compression, to determine the residual strength. A consistent relation between impact energy and CAI strength of composite laminates has been shown in previous studies [11–14].

Considerable experimental and computational work has been reported on the determination and prediction of CAI strength of post-impacted composite laminates under in-plane compressive loading [15–20]. With the aim of simplifying the experimental process, Asp et al. [21] performed compression tests on composite panels with embedded artificial delaminations, negating the need for impact tests. A comparison of results obtained from impacted and artificially delaminated samples showed that both types of samples failed due to the growth of delamination. The residual strengths of the two cases were similar but artificially delaminated samples presented higher stiffness than impacted samples. M. Remacha et al. [22] developed a new test fixture to determine the CAI strength of composite structures. Compared to the fixtures used in the American Society of Testing Materials (ASTM) D7137/7137 M standard, the benefit of this fixture was that it could be used to test thinner composite laminates which are prone to buckle during CAI tests [23,24].

Physical testing, which usually requires a large number of samples and operations, is costly and time consuming. This has driven the aerospace industry, in particular, to seek economically efficient means of structural testing through the increased use of simulation [25,26]. The research community has responded through efforts to develop robust damage models for reproducing the material response under various loading conditions. Rivallant et al. [27] developed a model for the numerical simulation of impact damage, permanent indentation and CAI in carbon-fibre reinforced composite laminates. The damage evolution during both low-velocity impact tests and CAI tests were captured by the same predictive model. This damage model

2

was also used to evaluate the effects of impact energy on the residual strength of composite laminates after impact. An investigation on the numerical prediction of CAI strength in woven composite laminates was carried out by Mendes and Donadon [14]. Two different modelling approaches, Single Shell Model (SSM) and Split Shell Model (SpSM), were used to build the computational model. Comparison between experimental and numerical results was conducted to evaluate the capability of these damage models in predicting the CAI strength of composite laminates. A high-fidelity three-dimensional composite damage model was presented by Tan et al. [12] to predict both low-velocity impact damage and CAI strength of composite laminates. This physically-based damage model was implemented as a user material subroutine in the commercial Finite Element (FE) package, Abaqus/Explicit. The virtual impact and CAI tests were conducted using the same FE model and the intralaminar damage features, delamination damage area and residual strength attained were in excellent agreement with experimental results.

In this work, the model presented in [12] was adopted and modified to enable the simulation of hybrid composites undergoing impact damage and subsequent compression testing. The physical impact and CAI tests, used for model validation, were conducted based on the ASTM D7316/7316M and ASTM D7317/7317M standards [9,28], respectively. C-scanning was performed to gain further insight into the evaluation of damage leading to catastrophic failure. The simulation results were in excellent correlation with the corresponding experiment results. The modelling enabled a quantitative assessment of the use of hybrid UD/woven carbon-fibre reinforced composites and an equivalent laminate which only consisted of UD plies.

2. Overview of the damage model

The failure modes presented by carbon-fibre reinforced composite laminates may be broadly classified into two categories: interlaminar (delamination) and intralaminar (matrix cracks and fibre pull-out/breakage) failure as shown in Fig. 1.
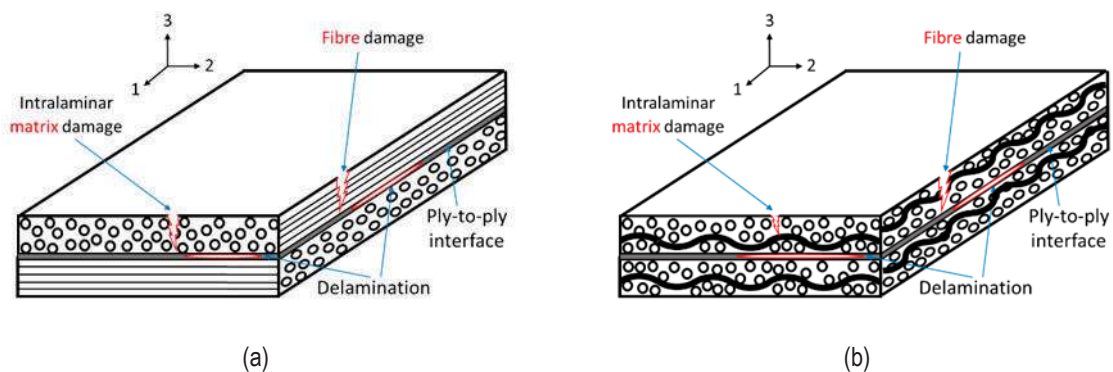

(a)   (b)

Fig. 1. Failure modes in (a) UD and (b) woven carbon-fibre reinforced composite laminates.

The damage model is a CDM [29,30] based smeared crack FE model. Details of this model have been reported in [12,31,32] and only a brief outline is included in this paper.

2.1 Intralaminar damage initiation

The damage response is assumed to be elastic in the longitudinal and transverse directions and inelastic in shear. Strain-based damage initiation functions, Eq. (1) and Eq. (2), are utilised to model the initial material response along the fibre direction,

$$F_{fib}^T(\varepsilon_{fib}) = \left(\frac{\varepsilon_{fib}}{\varepsilon_{fib}^{OT}}\right)^2 \geq 1 \tag{1}$$

$$F_{fib}^C(\varepsilon_{fib}) = \left(\frac{\varepsilon_{fib}}{\varepsilon_{fib}^{OC}}\right)^2 \geq 1 \tag{2}$$

where F_{fib}^T and F_{fib}^C are the failure indices for tension and compression, and the fibre failure initiation strains for tension and compression are represented by ε_{fib}^{OT} and ε_{fib}^{OC}, respectively. In this criterion, ε_{fib} is the current strain in the fibre direction, i.e. longitudinal for a UD ply but both longitudinal and transverse in a woven ply.

The initiation failure criteria developed according to the theories proposed by Puck and Schurmann [33] and Catalanotti [34] et al. were used to capture the transverse and through-thickness matrix-dominated damage initiation in a UD ply. The modified Hashin criterion [28], which can distinguish between various modes of failure and consider the interaction between normal stress (σ_{33}) and shear stress (τ_{13} and τ_{23}), was employed for the thorough-thickness damage initiation in a woven ply [35]. The matrix-dominated failure criteria are given bellow,

UD lamina:

$$F_{mat} = \left(\frac{\sigma_{NN}}{S_{23}^A}\right)^2 + \left(\frac{\sigma_{NT}}{S_{23}^A}\right)^2 + \left(\frac{\sigma_{LN}}{S_{12}^A}\right)^2 + \lambda\left(\frac{\sigma_{NN}}{S_{23}^A}\right)\left(\frac{\sigma_{LN}}{S_{12}^A}\right)^2 + \kappa\left(\frac{\sigma_{NN}}{S_{23}^A}\right) \ for \ \sigma_{NN} > 0 \tag{3}$$

$$F_{mat} = \left(\frac{\sigma_{NT}}{S_{23}^A - \mu_{NT}\sigma_{NN}}\right)^2 + \left(\frac{\sigma_{LN}}{S_{12}^A - \mu_{LN}\sigma_{NN}}\right)^2 \ for \ \sigma_{NN} \leq 0 \tag{4}$$

woven lamina:

4

$$F_{33}^T = \left(\frac{\sigma_{33}}{\sigma_{33}^{OT}}\right)^2 + \left(\frac{\tau_{13}}{\tau_{13}^O}\right)^2 + \left(\frac{\tau_{23}}{\tau_{23}^O}\right)^2 - 1 \geq 0, \sigma_{33} \geq 0 \qquad (5)$$

$$F_{33}^C = \left(\frac{\sigma_{33}}{\sigma_{33}^{OC}}\right) + \left(\frac{\tau_{13}}{\tau_{13}^O}\right)^2 + \left(\frac{\tau_{23}}{\tau_{23}^O}\right)^2 - 1 \geq 0, \sigma_{33} < 0 \qquad (6)$$

where F_{mat} is the failure index for matrix tensile and compressive failure. In Eq. (3) and (4), $\sigma_{ij}(i,j = N,T,L)$ are the stresses on the fracture surface of a UD lamina as shown in Fig. 2. Parameters κ and λ are defined by $\lambda = 2\mu_{LN}S_{23}^A/S_{12}^A - \kappa$, and $\kappa = (S_{12}^{A2} - (Y_T)^2)/S_{23}^A Y_T$, where S_{12}^A and S_{23}^A are the shear strengths. The transverse friction coefficients μ_{NT} and μ_{LN} are defined based on the Mohr-Coulomb theory where $\mu_{NT} = -1/tan(2\theta_f)$, $S_{23}^A = Y_C/2tan(\theta_f)$ and $\mu_{LN} = \mu_{NT}S_{12}^A/S_{23}^A$, Y_T and Y_C are the transverse tensile strength and transverse compressive strength, respectively. $F_{33}^{T(C)}$ are the tensile/compressive failure indices. σ_{33} is the normal stress, and τ_{ij} $(i,j = 1,2,3, i \neq j)$ are the shear stresses, in the through-thickness direction of a woven ply. $\sigma_{33}^{OT/OC}$ represent the matrix tensile/compressive strengths, and τ_{ij}^O $(i,j = 1,2,3, i \neq j)$ are the matrix shear strengths.
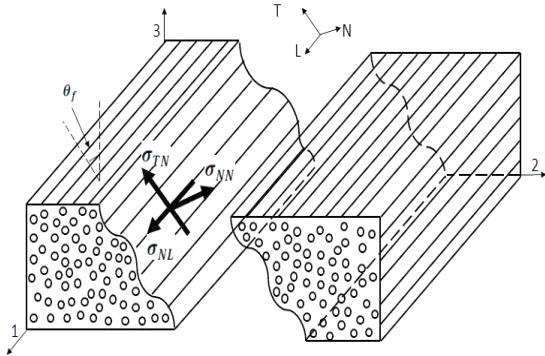

Fig. 2. Material coordinate system $(\mathbf{1,2,3})$ rotated to the fracture plane coordinate system $(\mathbf{L,N,T})$. [33]
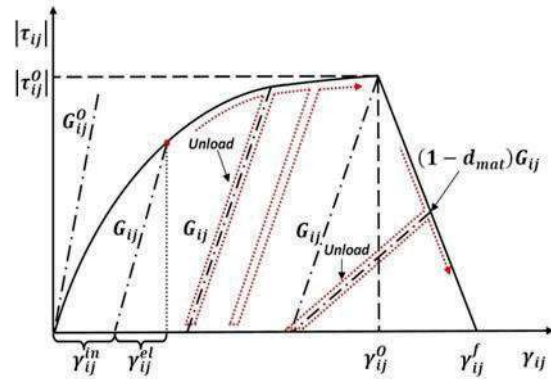

Fig. 3. Non-linear shear profile with different loading/unloading paths. [31]

2.2 Intralaminar damage evolution

Monotonically increasing damage variables each ranging from 0 (no damage) to 1 (complete failure) were used to represent the evolution of damage in the UD and woven plies. Every damage variable was related to a certain failure mode. Damage variables, d_{fib}^T and d_{fib}^C, refer to fibre-dominated tensile and compressive damage, respectively. d_{mat} indicates the evolution of matrix damage due to a combination of transverse tension/compression and shear loading,

$$d_{fib}^{T(C)} = \frac{\varepsilon_{fib}^{FT(C)}}{\varepsilon_{fib}^{FT(C)} - \varepsilon_{fib}^{OT(C)}}\left(1 - \frac{\varepsilon_{fib}^{OT(C)}}{\varepsilon_{fib}^{T(C)}}\right) \quad , \tag{7}$$

$$d_{mat} = \frac{\varepsilon_r^f - \varepsilon_{r,in}^0}{\varepsilon_r^f - \varepsilon_r^0}\left(1 - \frac{\varepsilon_r^0 - \varepsilon_r}{\varepsilon_r - \varepsilon_{r,in}^0}\right) \quad , \tag{8}$$

where the initiation strains, $\varepsilon_{fib}^{OT(C)}$ and $\varepsilon_{f(m)}^{OT(C)}$, are determined by the material strength $X_{fib}^{T(C)}$ and $X_{f(m)}^{T(C)}$. In Eq. (8), ε_r is the l^2-norm of strains acting on the fracture plane. $\varepsilon_{r,in}^0$ is the l^2-norm of inelastic strains at damage initiation. ε_r^0 and ε_r^f are the l^2-norms of strains corresponding to initial and final damage, respectively. The failure strain is defined by the respective critical energy release rate, $\Gamma^{T(C)}$, and the corresponding material strength, $X^{T(C)}$,

$$\varepsilon_{fib}^{FT(C)} = 2\Gamma_{fib}^{T(C)}/(X^{T(C)}l_{fib}) \quad , \tag{9}$$

where l_{fib} is the characteristic length associated with the longitudinal direction, and determined by $l_{fib} = V/A$, where V is the element volume and A is the representative fracture surface calculated using an approach in Tan et al. [12].

The shear response, required by the damage model, was obtained from standard V-notch shear tests and expressed as,

$$\tau(\gamma_{ij}) = c_1\left[exp(c_2\gamma_{ij}) - exp(c_3\gamma_{ij})\right] \quad , \tag{10}$$

where $c_i (i = 1, 2, 3)$ are coefficients, and $\gamma_{ij}(i, j = n, s, t, i \neq j)$ are the shear strains. Prior to damage initiation, shear loading and unloading occurs along gradients defined by the initial shear modulus G_{ij}. The damage propagation and nonlinear shear stress profiles are shown in Fig. 3.

In order to verify the implementation of the intralaminar damage model, virtual Modified Compact Tension (MCT) [36,37], Compact Compression (CC) [38,39] and virtual V-notched Rail Shear (VRS) [40,41] tests were simulated using the developed computational model according to the widely used testing protocols. The fibre-dominated tensile and compressive fracture toughness, and nonlinear properties, obtained from in-house material characterisation tests, were used in the verification models. The geometry, dimensions and laminate lay-ups of the model verification specimens are presented in Fig. 4 and Table 1. The loading direction was defined as the 0° direction. The material system used is IMS60/epoxy and the properties are

presented in Table 4. Comparison of load-displacement curves, obtained from experiment and computation, are shown in Figs. 5a, b and c, and are shown to be in good agreement.
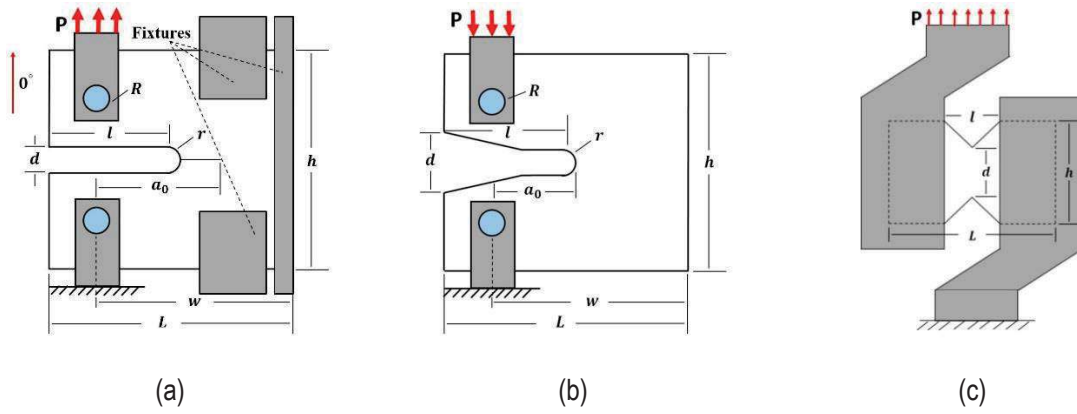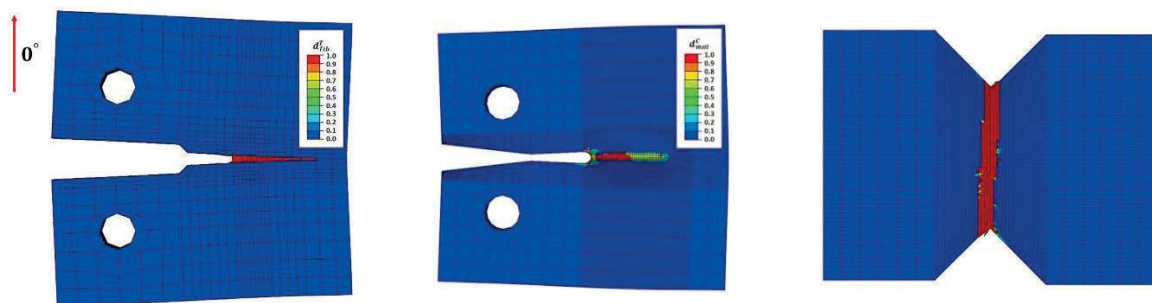

(a)   (b)   (c)

Fig. 4. Configuration for (a) MCT (b) CC and (c) VRS virtual tests.

Table 1

Dimensions of specimens for material characterisation (mm)

Samples	L	h	a_0	w	R	d	l	r	Lay-ups
MCT	65	60	26	51	4	4	28	2	$[(90/0)_s]_4$
CC	65	60	20	51	4	10	12	2	$[(90/0)_4]_s$
VRS	75	56	N/A	N/A	N/A	31	25	N/A	$[(0/90)_3]_s$

(a)   (b)   (c)
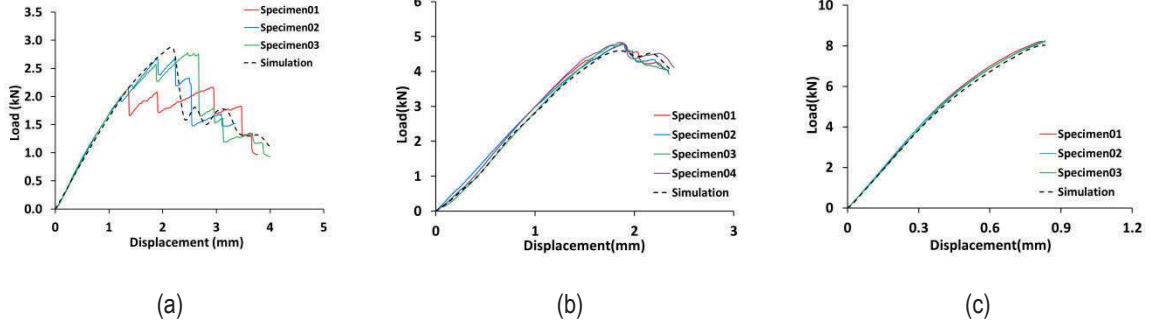
Fig. 5. (a) Virtual MCT test and load-displacement curves (b) virtual CC test and load-displacement curves and (c) virtual VRS test and load-displacement curves.

2.3 Interlaminar damage model

The built-in surface-based cohesive behaviour in Abaqus/Explicit was used to capture the delamination in composite structures using a bilinear traction-separation relationship. The interlaminar failure initiation is governed by a quadratic stress criterion,

$$\left(\frac{\tau_s}{\tau_s^0}\right)^2 + \left(\frac{\tau_t}{\tau_t^0}\right)^2 + \left(\frac{\langle\tau_n\rangle}{\tau_n^0}\right)^2 \leq 1 \quad , \tag{11}$$

where $\tau_i (i = n, s, t)$ is the normal direction and in-plane stresses respectively, and $\tau_i^0 (i = n, s, t)$ are the corresponding maximum stresses in each direction. In this model, the Benzeggagh–Kenane (B-K) propagation criterion [42] was used to propagate the delamination,

$$G_c = G_{Ic} + (G_{IIc} - G_{Ic})B^\eta \quad , \tag{12}$$

where G_c is the mixed-mode fracture toughness, and B is the local mixed-mode ratio defined as $B = G_{II}/G_I + G_{II}$. The parameter, η, is the mixed-mode interaction parameter determined from in-house experiments based on the ASTM D6671/D6671M-03 testing standard [43].

2.4 Model implementation

A VUMAT subroutine was developed for Abaqus/Explicit to predict the residual strength of post-impacted composite structures. The main subroutine contains three second-level subroutines to capture fibre-dominated failure, matrix-dominated failure and nonlinear shear behaviour. The overall subroutine flowchart is shown in Fig. 6.
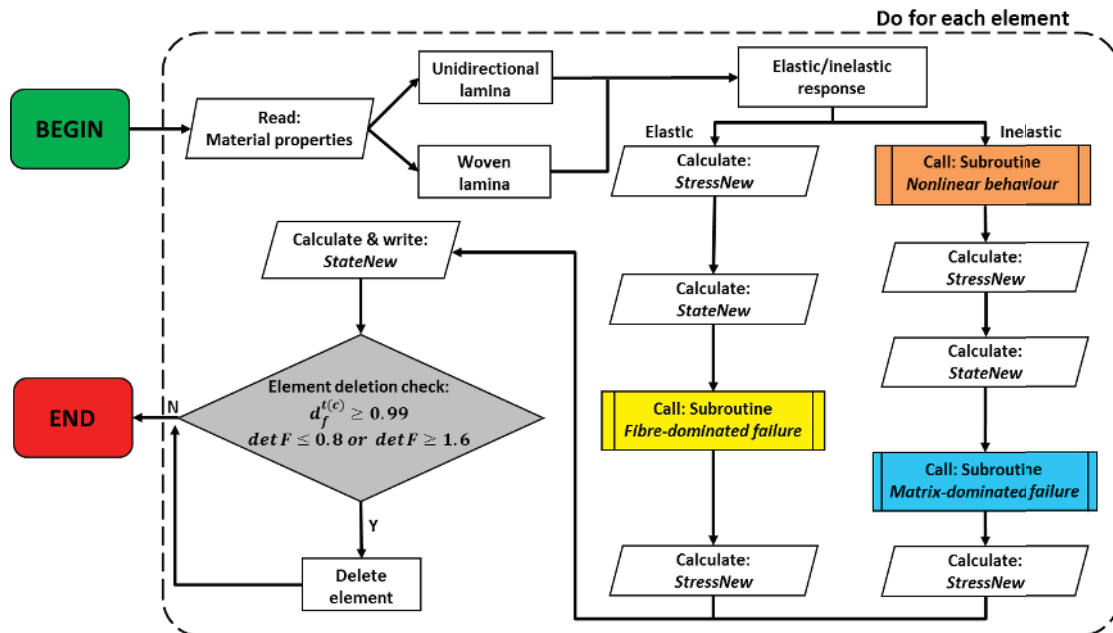

Fig. 6 . Flowchart of main VUMAT subroutine

3. Impact and CAI tests

The pristine panels for impact drop-weight tests were manufactured using Resin Infusion under Flexible Tooling (RIFT). All panels were subsequently inspected using a C-scan system to ensure the specimens were defect-free. The impact tests were carried out in an Instron-Dynatup 9250 HV drop-weight testing machine with a steel impactor with a hemispherical nose of 12.7 mm diameter. The impact energy was adjusted by changing the height of the impactor drop. The specimen was supported on a rigid platform and fixed by four clamps with rubber tips [44]. The testing apparatus is shown in Fig. 7a. The ASTM 7136/7136M test standard was adopted for performing the impact tests.

9
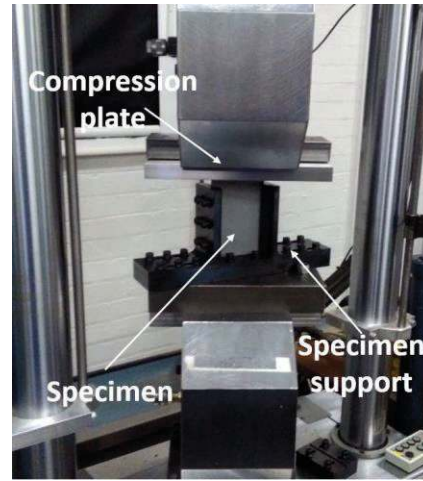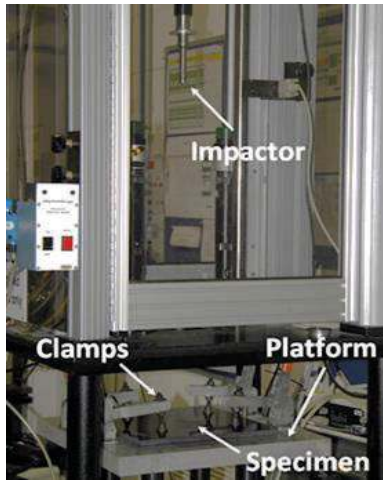
(a)   (b)

Fig. 7. Experimental set-up for (a) impact test and (b) CAI test.

A selection of post-impacted specimens was employed to conduct the CAI tests. The lay-ups, corresponding impact energy and dimensions are presented in Table 2.

Table 2

Geometric parameters and lay-up of the specimens for CAI test specimens.

Specimen code	Lay-up	Energy (J)	L (mm)	W (mm)	t (mm)
C-L1	[5HS/-45/+45/90/0/-45/+45/90/+45/-45/90/+45/-45/0/90/+45/-45/5HS]	25 17 10	150	100	4.78
C-L2	[5HS/0/0/+45/-45/0/0/0/-45/+45/0/0/0/+45/-45/0/0/5HS]	25 17 10	150	100	4.78

The CAI tests were carried out on a *Dartec* mechanical testing machine which can deliver a 250 kN maximum load. Displacement control was applied, and the testing speed was set at 1.25 mm/min following the ASTM D7317/7317M test standard. The experimental set-up for the CAI tests is presented in Fig. 7b.

4. Experimental results

4.1 Impact-induced damage

In this work, three different impact energy levels, 10 J, 17 J and 25 J, were used to generate the impact-induced initial damage in the CAI samples. For each composite lay-up, three samples were tested at each impact energy level. Fig. 8a shows the visible indentation on the top (impacted) surface of C-L2 specimens caused by an impactor with 25 J impact energy. The corresponding typical footprint of invisible damage, shown in Fig. 8b, was obtained through a C-scan system. A summary of measured experimental data, including average indentation, maximum length, maximum width and area of damage footprints, obtained from P#1 and P#2 specimens for different impact energy cases, are given in Table 3 [45].
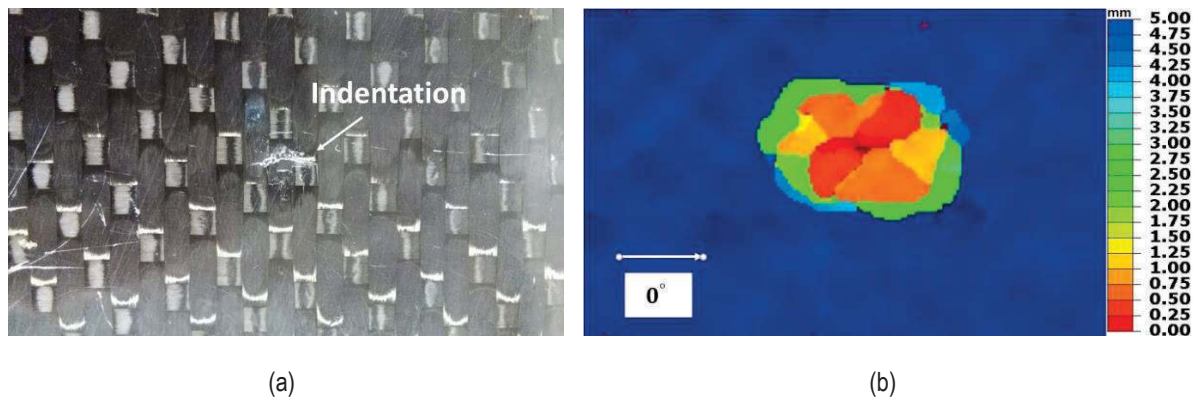

(a)   (b)

**Fig. 8** (a) Visible indentation and (b) internal damage in CAI specimens.

Table 3

Summary of experimental data measured from impact tests

Panel ID	Energy (J)	Average indentation depth(mm)	Maximum length (longitudinal) (mm)	Maximum width (transverse) (mm)	Delamination area (mm^2)
	25	0.22±10.1%	51.44±4.16%	50.76±4.64%	1904.7±2.73%
P#1	17	0.14±16.2%	41.82±6.15%	37.46±18.29%	1171.3±5.78%
	10	0.08±6.7%	29.11±10.15%	28.00±7.61%	625.6±10.59%
	25	0.19±18.9%	65.09±7.08%	36.92±5.36%	1831.7±5.21%
P#2	17	0.17±23.5%	45.06±4.97%	28.82±5.64%	1112.3±3.25%
	10	0.13±17.3%	33.77±7.21%	21.73±11.19%	610.4±6.16%

4.2 CAI test results

4.2.1 Visible damage

Following the CAI tests, the macroscale damage of the fractured specimens was investigated. The side view, front view and back view of the failed CAI samples are shown in Figs. 9a-c. CAI samples with different initial damage presented different degrees of damage under compressive loading. This difference may be characterised by the damage area encompassing intralaminar cracks, crush and delamination observed on one side of the sample. The 10J-impaced CAI samples, C-L1-10 and C-L2-10, presented more damage including larger delamination and local crush than the damage in those samples impacted at higher energy levels. In addition, a very clear intralaminar crack can be observed at the front and back of the tested CAI sample. The location of the dominant fracture surface of all CAI samples is similar and constant, which is close to the centre cross-section and propagated across the whole sample. Fig. 9c shows the catastrophic fracture from a 25J-impacted C-L2 specimens. Fig. 9d explains the damage morphology.

(a)   (b)

(c)   (d)
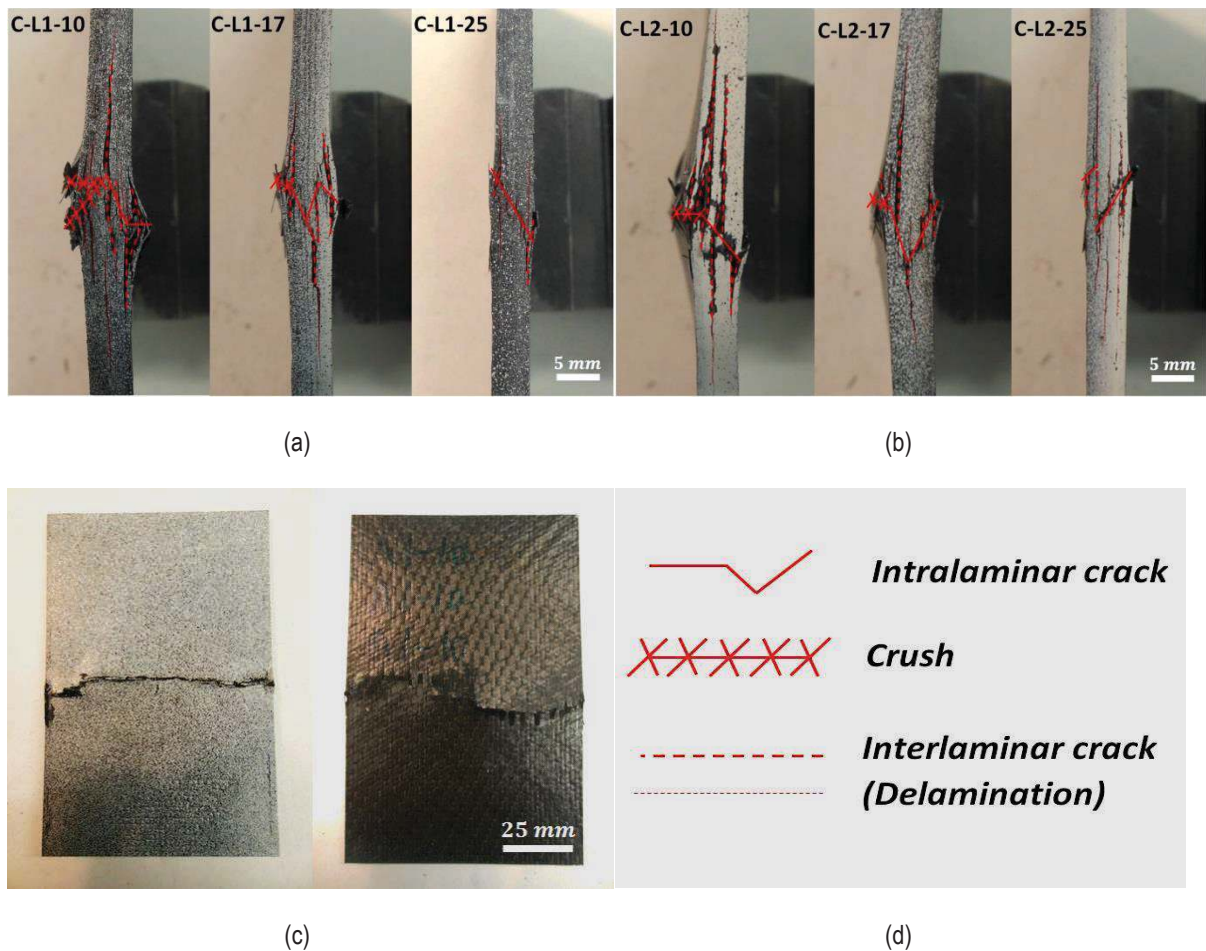
Fig. 9. The side view of damaged (a) C-L1 (b) C-L2 impacted specimens (c) typical front and back view of failed 25J-impacted specimen and (d) legend for illustration of morphology.

4.2.2 C-scan inspection

The tested CAI samples were inspected using a C-scan system and the obtained images are shown in Figs. 10a-f. In order to obtain a high-quality C-scan image, the damaged samples were flattened using an even compressive loading over the XY surface. As shown in the C-scan images, at the same impact energy level, the damaged area presented by C-L2 impacted specimens is larger than that observed in C-L1 impacted specimens. The C-L2 lay-up contains more 0° plies which promotes more delamination under longitudinal compression. In contrast, the C-L1 lay-up has more 90° plies which are able to constrain the delamination propagation. As a result, the delamination of C-L1 impacted specimens was constrained to a correspondingly narrow area along the transverse cross-section. For the same composite lay-up, the delamination area presents an inverse relation with the impact energy. For example, the 10J-impacted C-L1 impacted specimens delivered a larger delamination area than the 25J-impacted C-L1 impacted specimens.
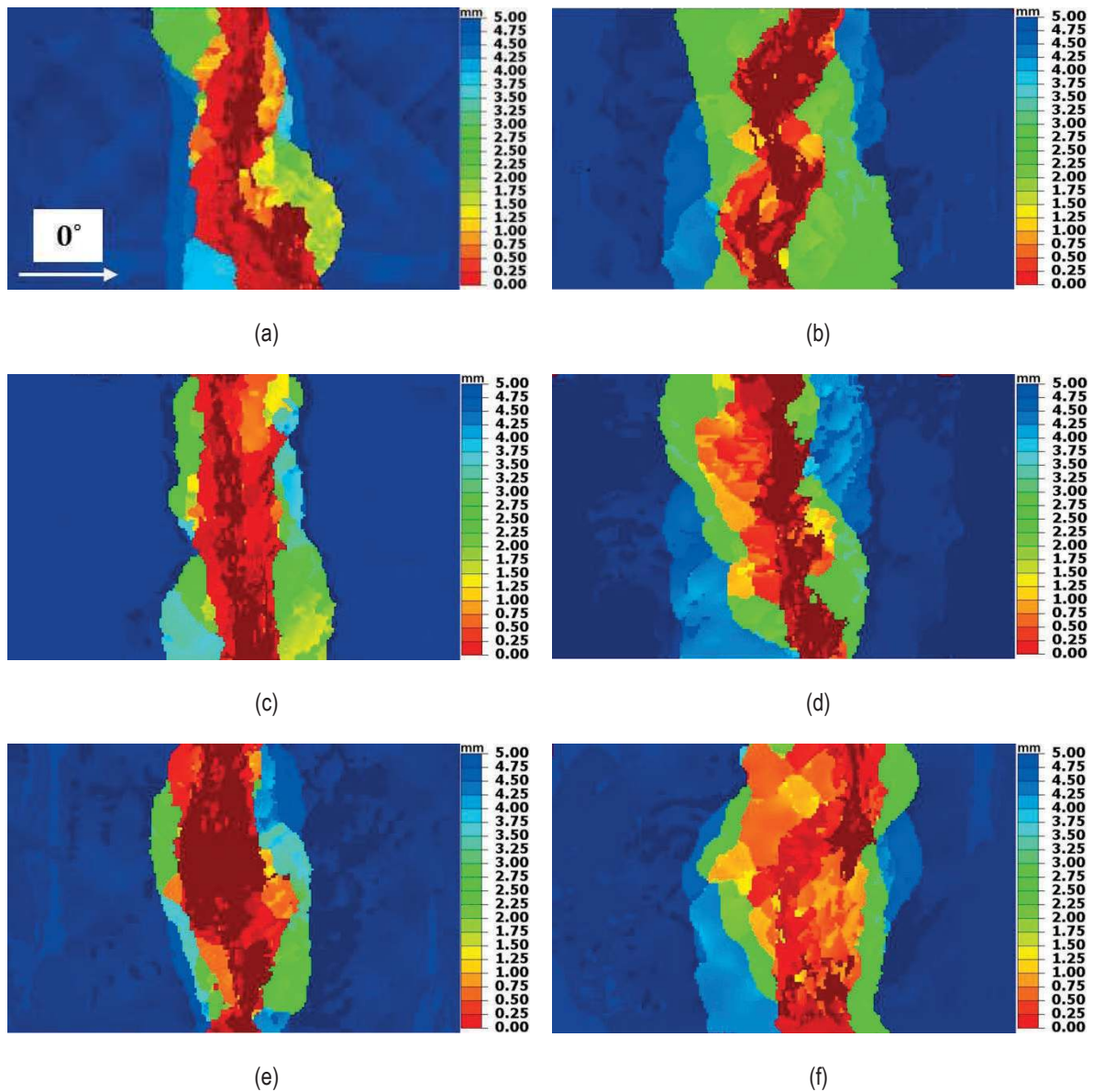

(a)

(b)

(c)

(d)

(e)

(f)

13

Fig. 10. The C-scan images obtained from (a) C-L1-10 (c) C-L1-17 (e) C-L1-25, and (b) C-L2-10 (d) C-L2-17 (f) C-L2-25 impacted specimens.

4.2.3 Global response

In the CAI tests, the nominal stress was calculated according to the measured maximum load and the transverse cross-sectional area. In Fig.11, all the nominal stress-displacement curves obtained from CAI specimens with different initial damage behave linearly before rapid catastrophe failure. The nominal stress-displacement curves obtained from pristine panels are included for comparison. It is readily observed that the higher the initial impact damage, the greater the stiffness and compressive strength reduction.

(a)

(b)
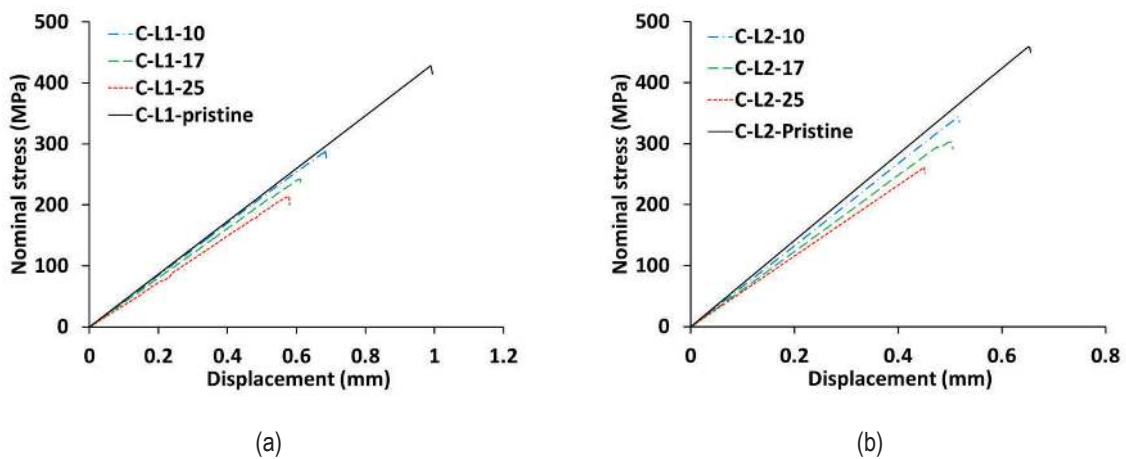
Fig. 11. Nominal stress-displacement curves obtained from (a) C-L1 and (b) C-L2 impacted specimens with different initial impact damage.

4.2.4 Residual strength

The residual strength decreased with increasing impact energy, Fig. 12a. Compared to C-L1 impacted specimens, the C-L2 impacted specimens that have a higher initial strength delivered a higher residual strength at the same impact energy level. This was primarily due to the five-fold increase in $0°$ plies in the C-L2 specimens. In Fig. 12b, the normalised residual strength of C-L1 and C-L2 impacted specimens are presented to indicate the ratio of residual strength to pristine strength.
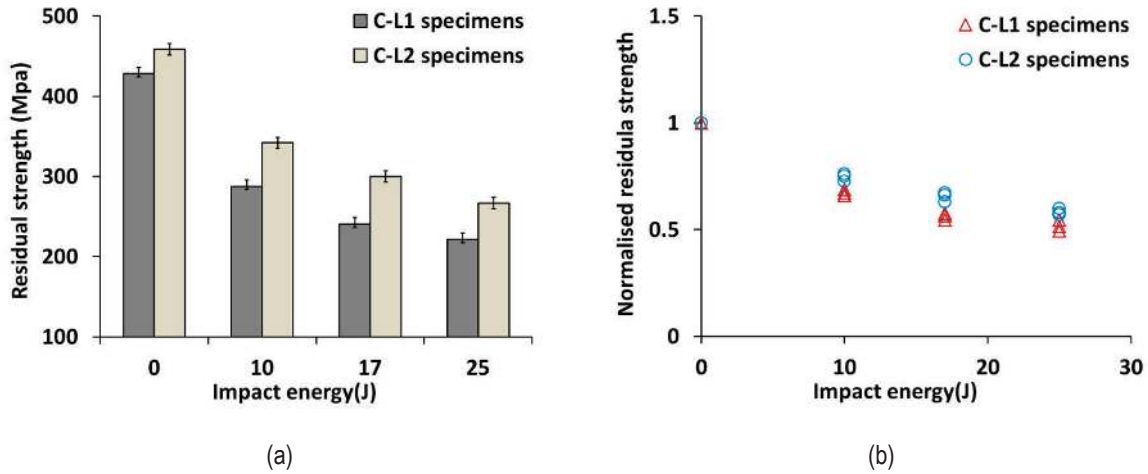
14

(a)   (b)

Fig. 12. (a) Residual strength versus impact energy and (b) normalised residual strength versus impact energy.

5. Finite element model

A finite element (FE) model was developed in Abaqus/Explicit to conduct the virtual CAI tests [12]. Prior to the CAI simulation, the drop-weight impact simulation was completed as shown in Fig. 13a. The impactor was modelled as a spherically-shaped analytical rigid surface, with a reference lumped mass of 6.4 kg, and the clamps were defined as a rigid body with a compressive preload to fix the panel. The impact-induced damage footprints obtained from C-scan measurements are compared with those predicted by simulation and shown in Fig. 13b. After the impact event, all the boundary conditions for the impact simulation were removed and new boundary conditions (Fig. 14) were applied for the CAI simulation in the FE model. In order to reduce the calculation time, the compressive load was set as 500mm/s whilst ensuring that the quality of the results was not affected by inertial effects [46]. To suppress spurious energy modes associated with the use of elements with reduced integration, an enhanced stiffness-based hourglass and distortion control were employed. The model was meshed with $1.5mm \times 1.5mm \times$ single-ply-thickness C3D8R elements. The general contact algorithm which is available in Abaqus/Explicit was used to simulate contact in the numerical model. A measured friction coefficient of 0.25 was used in the ply-to-ply contact. For the impactor-to-ply and clamp-to-ply contacts, a friction coefficient of 0.2 was used [47].

15

(a)   (b)
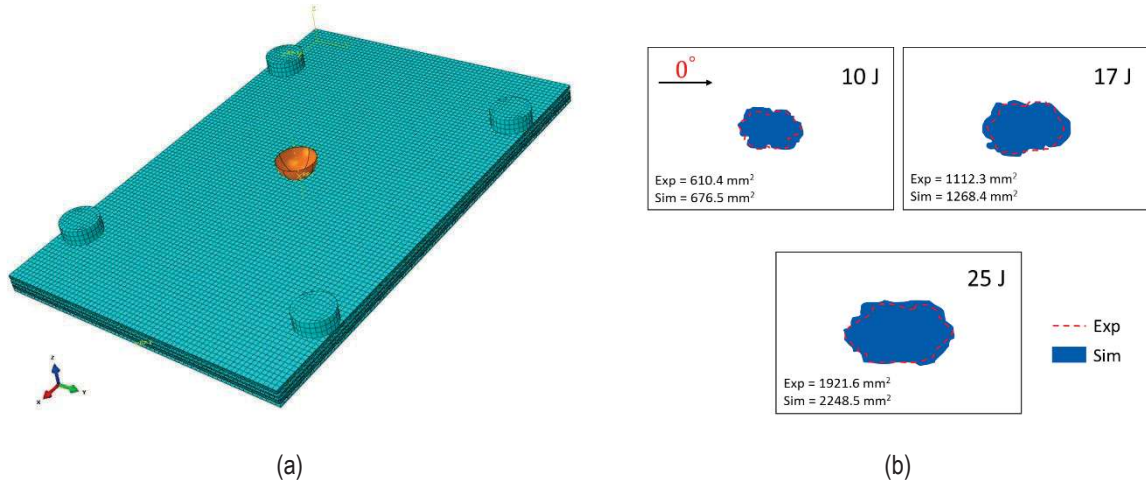
Fig. 13. (a) FE model for impact simulation and (b) comparison of damage footprints obtained from simulation and C-scan measurement for different impact energy levels.
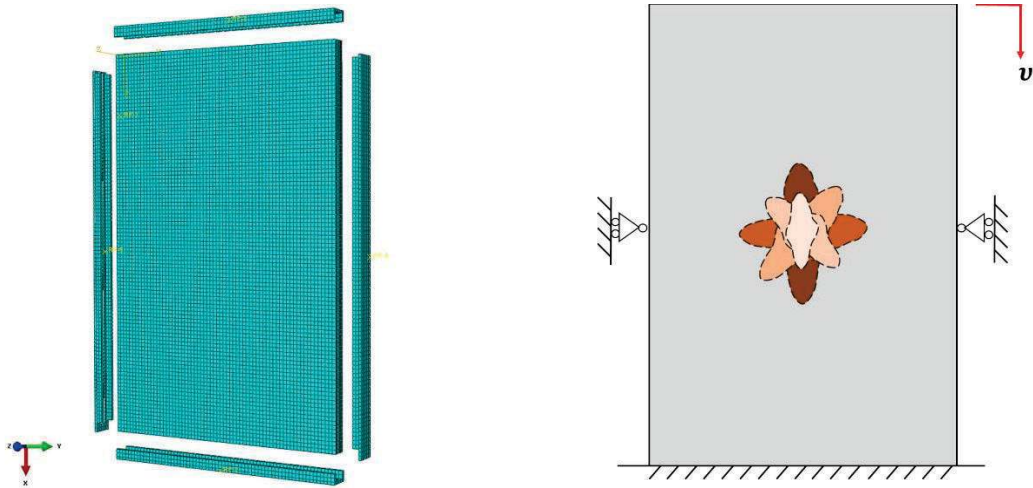
Fig. 14. (a) FE model for CAI simulation (b) boundary condition for virtual CAI tests.

The material systems used in the FE model are an IMS60/epoxy UD carbon-fibre/epoxy and AS4/epoxy woven carbon-fibre/epoxy laminated composite. The material properties for data reduction and numerical simulation were obtained using a series of in-house tests and are shown in Table 4. The intralaminar fracture energies associated with fibre-dominated tensile $(G_{Ic}|_{ft})$ and compressive $(G_{Ic}|_{fc})$ failure were measured from MCT and CC testing schemes [48,49]. The standard VRS testing method [50] was used to obtain the coefficients of c_1, c_2 and c_3, required in Eq. (10). The interlaminar fracture energies $(G_{Ic}$ and $G_{IIc})$, and B-K coefficient (η) were determined using standard DCB, four-point ENF and MMB tests [43,51–53].

Table 4

Mechanical properties of IMS 60/epoxy UD lamina and AS4/epoxy 5HS woven lamina

Materials	UD lamina	Woven lamina
Modulus (GPa)	$E_{11} = 152$; $E_{22} = E_{33} = 8.71$;	$E_{11} = E_{22} = 65.4$; $E_{33} = 8.71$;
	$G_{12} = G_{13} = 4.14$; $G_{23} = 3.35$;	$G_{12} = G_{13} = 3.59$; $G_{23} = 4.18$;
Poisson`s ratio	$\nu_{12} = \nu_{13} = \nu_{23} = 0.3$;	$\nu_{12} = \nu_{13} = \nu_{23} = 0.041$;
Strength (MPa)	$X^T = 1930$; $X^C = 962$;	$X^T = Y^T = 862$;
	$Y^T = 41.4$; $Y^C = 276$;	$X^C = Y^C = 689$;
	$S_{12} = 82.1$;	$S_{12} = 110$;
Intralaminar fracture energies (kJ/m^2)	$G_{Ic}|_{ft} = 775$; $G_{Ic}|_{fc} = 87$; [40,54]	$G_{Ic}|_{ft} = 201$; $G_{Ic}|_{fc} = 92$;
Non-linear shear properties	$c_1 = 66.5$; $c_2 = 3.2$; $c_3 = 62.4$;	$c_1 = 77.2$; $c_2 = 3.6$; $c_3 = 65.2$;
Interlaminar fracture energies (kJ/m^2)	$G_{Ic} = 0.46$; $G_{IIc} = 1.51$;	$G_{Ic} = 0.32$; $G_{IIc} = 2.01$;
B-K coefficient	$\eta = 1.89$	$\eta = 2.09$

6. Model validation

6.1 Load-displacement curves

For brevity, only the experimental results obtained from C-L2 impacted specimens are presented to demonstrate the validation of the proposed damage model. Both strength and stiffness reduction were accurately captured by the proposed damage model and excellent correlation was achieved between the physical tests and numerical simulation, Fig. 15.
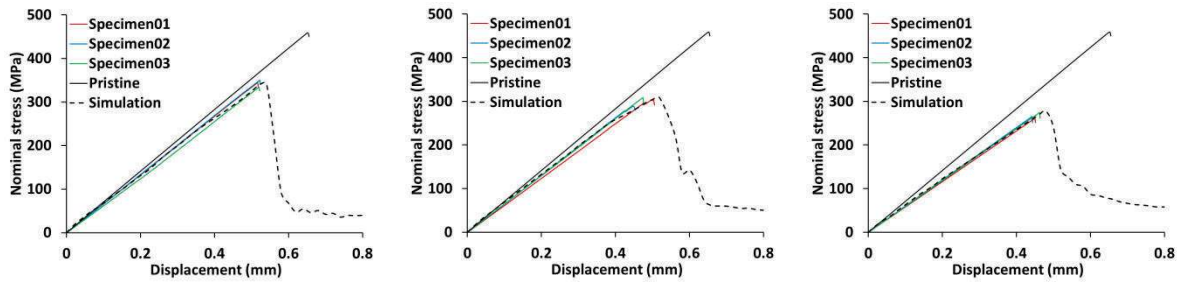
Fig. 15. Load-displacement curves obtained from C-L2 specimens for (a) 10J (b) 17J and (c) 25J impact energy.

Fig. 16 depicts the evolution of different types of damage obtained from the C-L2-25J impacted specimen in the virtual CAI

test. As shown in the figure, energy dissipation due to interlaminar and intralaminar damage increased sharply when the load

reached its maximum value. Intralaminar damage consumed most (around 56%) of the absorbed energy. Interlaminar damage

also played an important role in the energy dissipation of the CAI event.
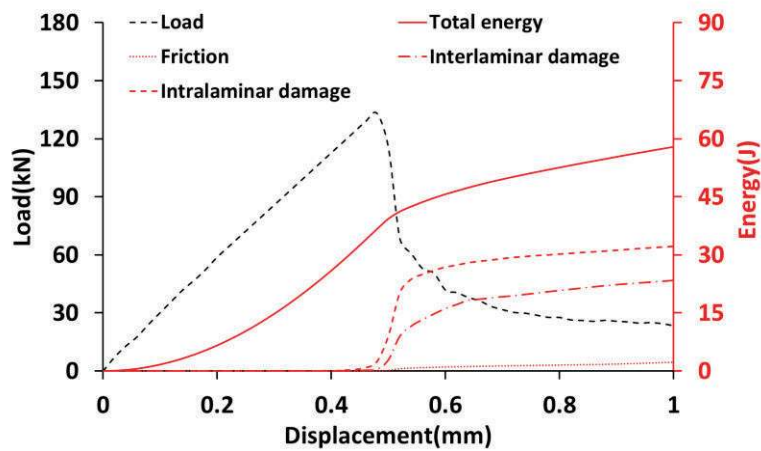
Fig. 16. Energy dissipation in a CAI event for C-L2-25J-impacted sample.

6.2 Damage due to compressive loading

Fig. 17a shows the footprint of CAI damage in the C-L2-25J impacted specimen obtained from simulation. The damage contour

obtained from simulation was compared to experimental results as shown in Fig. 17b. The simulation results presented more

damage in the central area than the fringe area on the composite panel. The footprint area obtained by simulation is slightly

less than the area presented by the C-scan results, while the main damage area obtained from C-scan was accurately

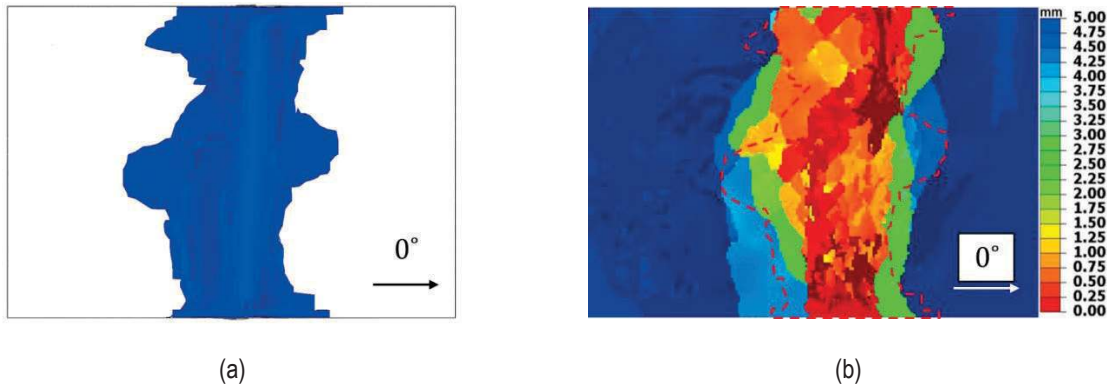reproduced by the numerical simulation using the proposed damage model.

18

(a)   (b)

Fig. 17. (a) Damage footprint of C-L2-25J impacted specimen attained from simulation and (b) comparison of damage footprints obtained from experiment and simulation.

6.3 Performance assessment

In order to explore potential structural advantages of hybrid UD/woven carbon-fibre reinforced composite laminates, commonly used in the aerospace industry reasons given earlier, the fully validated computational model was used to compare the performances of UD-only carbon-fibre reinforced composite laminates and hybrid carbon-fibre reinforced composite laminates in a CAI test. The top and bottom sublaminates (5HS) of the lay-up [5HS/0/0/+45/-45/0/0/0/-45/+45/0/0/0/+45/-45/0/0/5HS] were substituted by a same thickness cross-ply (0/90) laminate, [(0/90)/0/0/+45/-45/0/0/0/-45/+45/0/0/0/+45/-45/0/0/ (90/0)], Fig. 18.
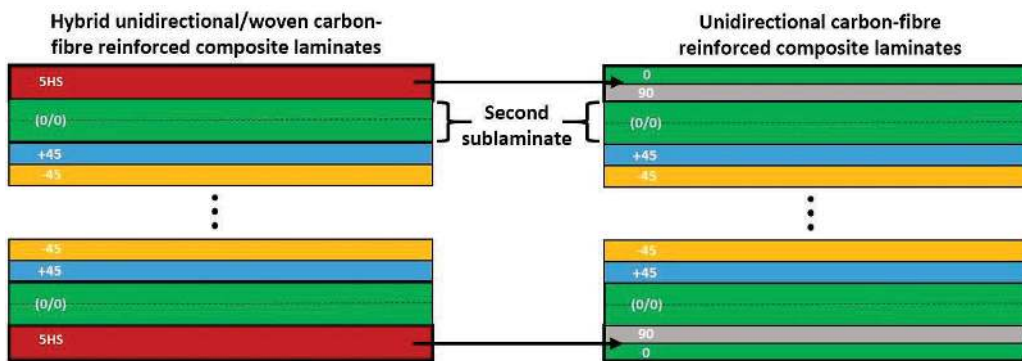

Fig. 18. Equivalent UD-only and hybrid laminates.

The virtual CAI test was carried out on the UD-only carbon-fibre reinforced composite laminate with 25 J impact energy and is referred to as the U-CAI-25J impacted specimen. The 25J-impacted hybrid carbon-fibre reinforced composite laminate is referred to as the U/W-CAI-25J impacted specimen. The nominal compressive stress-displacement curves obtained for these

19

two laminates is shown in Fig. 19. The maximum stress obtained from U/W-CAI-25J impacted specimen was 277.4 MPa, which is marginally higher (+3.3%), yet measurable, than that presented by U-CAI-25J impacted specimen (268.6 MPa).
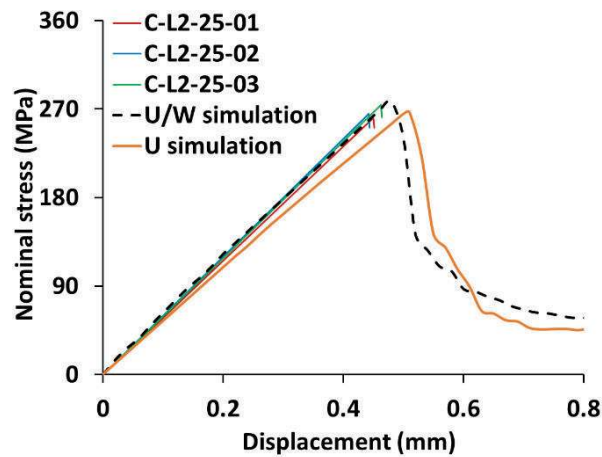

Fig. 19. Comparison of nominal compressive stress-displacement curves for U/W-CAI-25J and U-CAI-25J impacted specimens.

Details of the energy dissipation in the virtual CAI tests for the U-CAI-25J impacted specimen are shown in Fig. 20a. In order to compare the energy absorption capability of U/W-CAI-25J and U-CAI-25J impacted specimens, the values of absorbed energy obtained from the CAI simulation for U/W-CAI-25J and U-CAI-25J impacted specimens were compared and shown in Fig. 20b. The value of absorbed total energy obtained from the CAI simulation on the U/W-CAI-25J specimen was 57.9 J, which is 8.84% higher than that obtained from U-CAI-25J impacted specimen (53.2 J). In terms of energy dissipated by interlaminar damage, the values delivered by the U/W-CAI-25J impacted specimen (23.4 J) and the U-CAI-25J impacted specimen (22.9 J) are similar, while the U/W-CAI-25J impacted specimen presented 14.6% higher intralaminar damage energy (32.2 J) than the U-CAI-25J impacted specimen (28.1 J).
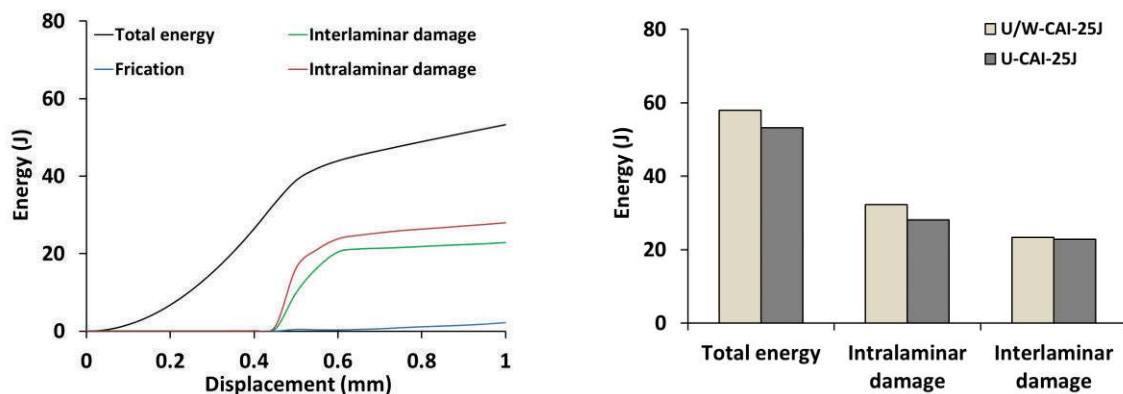
Fig. 20. (a) Energy dissipation in CAI event for U-CAI-25J samples and (b) comparison of absorbed energy between U/W-CAI-25J specimens and U-CAI-25J specimens.

The side-views of both post-CAI specimens obtained from the simulations are shown in Fig. 21. The U-CAI-25J impacted specimen presented more matrix damage and larger deformation than U/W-CAI-25J impacted specimen. Most of damage presented by the U-CAI-25J impacted specimen appeared in the outer layers which consist of UD composite plies. In Fig. 22, the comparison of damage footprints showed the total damage areas of U/W-CAI-25J impacted specimens and U-CAI-25J impacted specimen are very similar. The difference is the U/W-CAI-25J impacted specimen presented a more even damage distribution, while, the U-CAI-25J impacted specimen exhibited more damage in the central region.
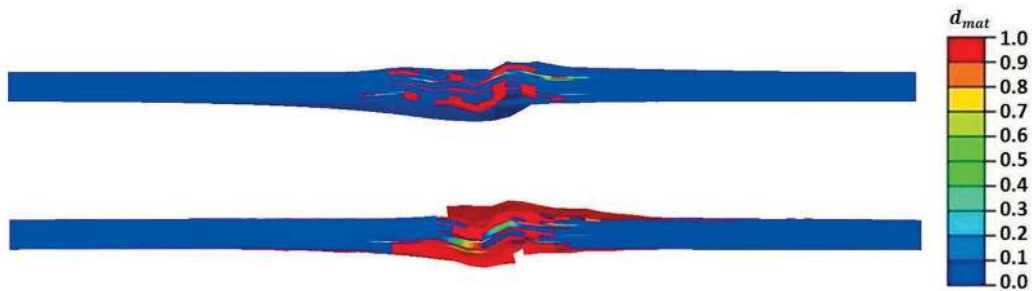
Fig. 21. Side-view of intralaminar matrix damage obtained from U/W-CAI-25J-impacted specimens (top) and U-CAI-25J specimens (bottom).

(a)   (b)
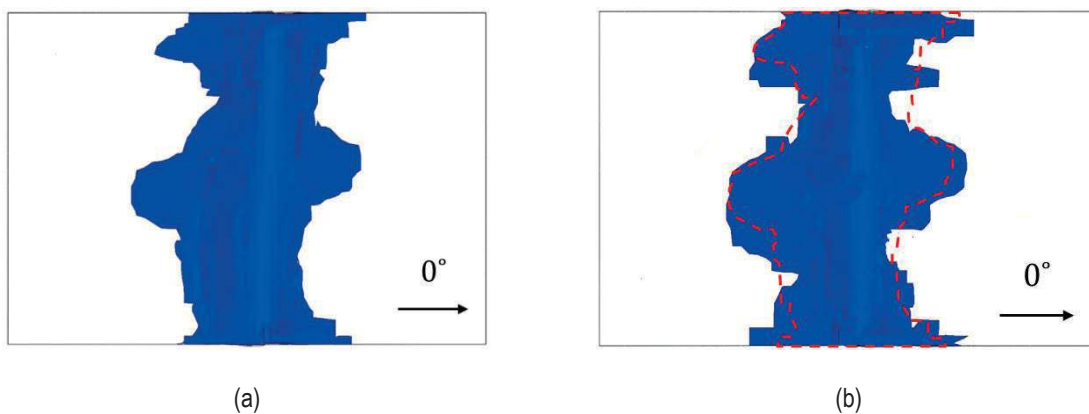
Fig. 22. Damage footprints of (a) U/W-CAI-25J-impacted specimens and (b) U-CAI-25J-impacted specimens.

6. Conclusions

21

This work presented an investigation into the predictive capability of a computation model to capture the residual strength of damaged hybrid UD/woven composite laminates under compressive loading. Initial impact damage was introduced into the FE model by simulating the low velocity impact event prior to the CAI simulation. An experimental investigation on the CAI strength of hybrid UD/woven carbon-fibre/epoxy composite laminates was carried out to validate the proposed damage model. Two different composite laminate lay-ups were used to conduct the low velocity impact and CAI tests. The global response and delamination images of composite laminates due to low velocity impact were obtained. The post-impacted samples with different degrees of impact damage were tested under compressive loading. Excellent correlation between physical tests and virtual tests was obtained, which indicated the reliable capability of the proposed model in capturing the response of composite laminates under compressive loading.

Furthermore, a comparative performance assessment was carried out on the hybrid UD/woven composite laminates and an equivalent UD-only composite laminate using the fully validated predictive model. The results showed that the use of woven plies on the surfaces of a laminate had a small, but measurable, positive influence on the residual strength of composite laminates in a CAI test.

Reference

[1]   Eyer G, Montagnier O, Hochard C, Charles J. Effect of matrix damage on compressive strength in the fiber direction for laminated composites. Compos Part A Appl Sci Manuf, 2017;94:86–92.
[2]   Moura MFSF de, Goncßalves JPM, Marques AT, Castro PMST de. Prediction of compressive strength of carbon-epoxy laminates containing delamination by using a mixed-mode damage model. Compos Struct, 2000;50:151–7.
[3]   Cantwell WJ, Curtis PT, Morton J. An assessment of the impact performance of CFRP reinforced with high-strain carbon fibres. Compos Sci Technol, 1986;25:133–48.
[4]   Hogg PJ, Prichard JC. The role of impact damage in post-impact compression testing. Composites, 1990;21:503–11.
[5]   Ishikawa T, Sugimoto S, Matsushima M, Hayashi Y. Some experimental findings in compression-after-impact (CAI) tests of CF/PEEK (APC-2) and conventional CF/epoxy flat plates. Compos Sci Technol, 1995;55:349–63.

22

[6] Soutis C, Curtis PT. Prediction of the post-impact compressive strength of CFRP laminated composites. Compos Sci Technol, 1996;56:677–84.

[7] Khondker OA, Leong KH, Herszberg I, Hamada H. Impact and compression-after-impact performance of weft-knitted glass textile composites. Compos Part A Appl Sci Manuf, 2005;36:638–48.

[8] Dogan A, Arikan V. Low-velocity impact response of E-glass reinforced thermoset and thermoplastic based sandwich composites. Compos Part B Eng, 2017;127:63–9.

[9] ASTM. Standard Test Method for Compressive Residual Strength Properties of Damaged Polymer Matrix Composite Plates. D7137/D7137M-12, West Conshohocken, PA, 2012.

[10] Airbus Standard. Determination of Compression Strength after Impact. AITM 1-0010, 2010.

[11] Falzon BG, Tan W. Predicting Impact Damage, Residual Strength and Crashworthiness of Composite Structures. SAE Int J Mater Manuf, 2016;9:718–28.

[12] Tan W, Falzon BG, Chiu LNS, Price M. Predicting low velocity impact damage and Compression-After-Impact (CAI) behaviour of composite laminates. Compos Part A Appl Sci Manuf, 2015;71:212–26.

[13] Dale M, Acha BA, Carlsson LA. Low velocity impact and compression after impact characterization of woven carbon/vinylester at dry and water saturated conditions. Compos Struct, 2012;94:1582–9.

[14] Mendes PAAE, Donadon MV. Numerical prediction of compression after impact behavior of woven composite laminates. Compos Struct, 2014;113:476–91.

[15] Bull DJ, Spearing SM, Sinclair I. Observations of damage development from compression-after-impact experiments using ex situ micro-focus computed tomography. Compos Sci Technol, 2014;97:106–14.

[16] Cartié DDR, Irving PE. Effect of resin and fibre properties on impact and compression after impact performance of CFRP. Compos Part A Appl Sci Manuf, 2002;33:483–93.

[17] Davies GAO, Hitchings D, Besant T, Clarke A, Morgan C. Compression after impact strength of composite sandwich panels. Compos Struct, 2004;63:1–9.

[18] Ghelli D, Minak G. Low velocity impact and compression after impact tests on thin carbon/epoxy laminates. Compos Part B Eng, 2011;42:2067–79.

[19] Habib FA. A new method for evaluating the residual compression strength of composites after impact. Compos Struct, 2001;53:309–16.

[20] Kazemahvazi S, Nilsson M, Zenkert D. Residual strength of GRP laminates with multiple randomly distributed fragment impacts. Compos Part A Appl Sci Manuf, 2014;60:66–74.

[21] Asp LE, Soren N, Singh S. An experimental investigation of the influence of delamination growth on the residual strength of impacted laminates. Compos Part A Appl Sci Manuf, 2001;32:1229–35.

[22] Remacha M, Sánchez-Sáez S, López-Romano B, Barbero E. A new device for determining the compression after impact strength in thin laminates. Compos Struct, 2015;127:99–107.

[23] Zhang X, Davies G, Hitchings D. Impact damage with compressive preload and post-impact compression of carbon composite plates. Int J Impact Eng, 1999;22:485–509.

[24] Zhang X, Hounslow L, Grassi M. Improvement of low-velocity impact and compression-after-impact performance by z-fibre pinning. Compos Sci Technol, 2006;66:2785–94.

[25] Papanicolaou GC. New approach for residual compressive strength prediction of impacted CFRP laminates. Compos Part A Appl Sci Manuf, 1995;26:517–23.

[26] Topac OT, Gozluklu B, Gurses E, Coker D. Composites : Part A Experimental and computational study of the damage process in CFRP composite beams under low-velocity impact. Compos Part A Appl Sci Manuf, 2017;92:167–82.

[27] Rivallant S, Bouvet C, Hongkarnjanakul N. Failure analysis of CFRP laminates subjected to compression after impact: FE simulation using discrete interface elements. Compos Part A Appl Sci Manuf, 2013;55:83–93.

[28] ASTM. Standard Test Method for Measuring the Damage Resistance of a Fiber-Reinforced Polymer Matrix Composite to a Drop-Weight Impact Event. D7136/D7136M-05, West Conshohocken, PA, 2005.

[29] Kachanov LM. Introduction to continuum damage mechanics. Boston: Martinus Nijhoff Publishers; 1986.

[30] Lemaitre J, Chaboche JL. Mechanics of solid materials. Cambridge: Cambridge University Press; 1990.

[31] Donadon M V., Iannucci L, Falzon BG, Hodgkinson JM, de Almeida SFM. A progressive failure model for composite laminates subjected to low velocity impact damage. Comput Struct, 2008;86:1232–52.

[32] Falzon BG, Liu H, Tan W. Comment on A tensorial based progressive damage model for fiber reinforced polymers. Compos Struct, 2017;176:877–82.

[33] Puck A, Schürmann H. Failure analysis of FRP laminates by means of physically based phenomenological models. Compos Sci Technol, 1998;58:1045–67.

[34] Catalanotti G, Camanho PP, Marques AT. Three-dimensional failure criteria for fiber-reinforced laminates. Compos Struct, 2013;95:63–79.

23

[35] Kaddour AS, Hinton MJ. Maturity of 3D failure criteria for fibre-reinforced composites: Comparison between theories and experiments: Part B of WWFE-II. J Compos Mater, 2013;47:925–66.

[36] Pinho ST, Robinson P, Iannucci L. Fracture toughness of the tensile and compressive fibre failure modes in laminated composites. Compos Sci Technol, 2006;66:2069–79.

[37] Catalanotti G, Camanho PP, Xavier J, Dávila CG, Marques AT. Measurement of resistance curves in the longitudinal failure of composites using digital image correlation. Compos Sci Technol, 2010;70:1986–93.

[38] Bru T, Hellstrom P, Gutkin R, Ramantani D, Peterson G. Characterisation of the mechanical and fracture properties of a uni-weave carbon fibre/epoxy non-crimp fabric composite. Data Br, 2016.

[39] Tan W, Falzon BG, Price M, Liu H. The role of material characterisation in the crush modelling of thermoplastic composite structures. Compos Struct, 2016;153:914–27.

[40] Tan W, Falzon BG. Modelling the nonlinear behaviour and fracture process of AS4/PEKK thermoplastic composite under shear loading. Compos Sci Technol, 2016;126:60–77.

[41] Fanteria D, Panettieri E. A non-linear model for in-plane shear damage and failure of composite laminates. Aerotec Missili Spaz, 2014;93:17–24.

[42] Benzeggagh ML, Kenane M. Measurement of mixed-mode delamination fracture toughness of unidirectional glass/epoxy composites with mixed-mode bending apparatus. Compos Sci Technol, 1996;56:439–49.

[43] ASTM. Standard Test Method for Mixed Mode I-Mode II Interlaminar Fracture Toughness of Unidirectional Fiber Reinforced Polymer Matrix Composites. D6671/D 6671M-03, West Conshohocken, PA, 2003.

[44] Aktaş M, Atas C, İçten BM, Karakuzu R. An experimental investigation of the impact response of composite laminates. Compos Struct, 2009;87:307–13.

[45] Liu H, Falzon BG, Tan W. Experimental and numerical studies on the impact response of damage-tolerant hybrid unidirectional/woven carbon-fibre reinforced composite laminates. Compos Part B Eng (2007), doi 101016/j.compositesb201710016.

[46] Tan W, Falzon BG. Modelling the crush behaviour of thermoplastic composites. Compos Sci Technol, 2016;134:57–71.

[47] Chiu LNS, Falzon BG, Chen B, Yan W. Validation of a 3D damage model for predicting the response of composite structures under crushing loads. Compos Struct, 2016;147:65–73.

[48] Chishti M, Wang CH, Thomson RS, Orifici AC. Characterising fibre compression fracture toughness of composites using bearing tests. Compos Part A Appl Sci Manuf, 2012;43:1775–82.

[49] Li X, Hallett SR, Wisnom MR, Zobeiry N, Vaziri R, Poursartip A. Experimental study of damage propagation in Over-height Compact Tension tests. Compos Part A Appl Sci Manuf, 2009;40:1891–5.

[50] ASTM. Standard Test Method for Shear Properties of Composite Materials by V-Notched Rail Shear Method. D7078/D7078M-05, West Conshohocken, PA, 2005.

[51] ASTM. Standard Test Method for Mode I Interlaminar Fracture Toughness of Unidirectional Fiber-Reinforced Polymer Matrix Composites. D5528-01, West Conshohocken, PA, 2004.

[52] ASTM. Standard Test Method for Determination of the Mode II Interlaminar Fracture Toughness of Unidirectional Fiber-Reinforced Polymer Matrix Composites. D7905/D7905M-14, West Conshohocken, PA, 2014.

[53] Schuecker C, Davidson BD. Evaluation of the accuracy of the four-point bend end-notched flexure test for mode II delamination toughness determination. Compos Sci Technol, 2000;60:2137–46.

[54] Marín L, González EV, Maimí P, Trias D, Camanho PP. Hygrothermal effects on the translaminar fracture toughness of cross-ply carbon/epoxy laminates: Failure mechanisms. Compos Sci Technol, 2016;122:130–9.

24